science.sciencemag.org/cgi/content/full/science.aax3873/DC1

Supplementary Material for

Type-II Ising pairing in few-layer stanene

Joseph Falson, Yong Xu, Menghan Liao, Yunyi Zang, Kejing Zhu, Chong Wang, Zetao Zhang, Hongchao Liu, Wenhui Duan, Ke He, Haiwen Liu*, Jurgen H. Smet*, Ding Zhang*, Qi-Kun Xue

*Corresponding author. Email: haiwen.liu@bnu.edu.cn (H.L.); j.smet@fkf.mpg.de (J.H.S.); dingzhang@mail.tsinghua.edu.cn (D.Z.)

Published 12 March 2020 as *Science* First Release
DOI: 10.1126/science.aax3873

This PDF file includes:

Materials and Methods
Supplementary Text
Figs. S1 to S8
Table S1
References

Materials

Heterostructures were fabricated by molecular beam epitaxy *(18)*. A five quintuple layer Bi_2Te_3(111) buffer film was initially deposited on a Si(111) substrate, followed by an *n*-layer (n=6,12,15) PbTe(111) film. On this substrate, *n* (n=2,3,5) atomic layers of Sn were deposited at low temperature ($T \approx 150$ K) and subsequently annealed at $T \leq 400$ K to improve the surface morphology. The reflected high energy electron diffraction (RHEED) pattern displayed a streak-pattern with no detectable shift during the growth, suggesting epitaxial locking of the stanene layer with the PbTe layer. The estimated lattice constant is $a = 4.52$Å.

Methods

All resistance data were obtained by standard low-frequency lock-in techniques. The data presented in Figure 2 **C** were collected in a ^{3}He cryostat operated down to $T = 250$ mK. All other low temperature data were gathered in a Top-Loading-into-Mixture (TLM) dilution refrigerator with a base temperature $T \approx 20$ mK. The samples were immersed in the ^{3}He-^{4}He mixture and mounted on a low-friction rotation stage to obtain both $B_\perp$ and $B_{//}$-data sets. The temperature of the ^{3}He-^{4}He mixture was read by a calibrated ruthenium oxide thermometer placed on the mixing chamber. The data shown in Fig. 2 and Fig. S3 **B** were recorded by sweeping the magnetic field from high field to zero. We estimate an error in the angle of 0.3^o from the perfectly parallel field orientation. The upper critical fields of 3-Sn/12-PbTe presented in Fig. 3 **A** are obtained from the position where the resistance drops to half of its normal state resistance. The temperature dependent upper critical field data of 3-Sn/6-PbTe in Fig. 3 **A** and those in Fig. 3 **B** are obtained from the resistance data presented in Fig. S4 **B**, S5 **B**, S6 **B**. These sets of data were collected by sweeping the rotation angle in steps of 0.05^o through the parallel configuration at a fixed total magnetic field and temperature while recording the resistance. Fig. S2 illustrates how this measurement was done. The right panel in Fig. S2 shows the resistance recorded as a function of the angle θ_{raw} (not calibrated, i.e. corrected for an offset). The resistance minimum in each trace at a different angle forms one data point in the ($B_{//}$-T)-plane on the left, as indicated by the horizontal dotted lines for some of the data points. By carrying out the measurement in this fashion, the angular precision is improved to 0.1^o. The data is interpolated in the left panel. The in-plane upper critical field is then obtained from the position where the interpolated resistance drops to half (or 1%) of the normal state resistance. The vertical error bars in Fig. 3, Fig. S6 **D** and Fig. S7

arise from half of the magnetic field step size (0.05 T). In other figures, the error bars are smaller than the size of the symbol.

Supplementary Text

I. Filtering of the measurement system

Ultra-low temperature measurements were performed in a TLM dilution refrigerator designed to enable low electron temperatures by effectively filtering high frequency signals and immersing the sample directly into the mixture. Recent reports *(29)* studying 2D superconductors have shown that these samples are extremely sensitive to external noise, necessitating thorough high frequency filtering of lines in order to accurately characterize the superconducting state. In the experimental setup, each measurement wire initially passes a damped LC filter stage within the breakout box at room temperature. Figure S1**A** displays the attenuation characteristics of this first filter. After entering the sample rod, the signal is carried from room temperature down to the 1K pot using individual thermocoax lines, each with a length of approximately 2.5 m. These lines consist of a resistive stainless steel inner conductor ($R_{\text{cable}} \approx 200\ \Omega$) that is isolated from the outer conductor by a MgO dielectric. High frequency signals are strongly attenuated along these lines owing to the skin effect of the MgO nanoparticles. These cables essentially act as efficient distributed RC filters and are therefore widely employed in cryogenics for suppressing stray radiation induced thermal fluctuations *(30)(31)*. Figure S1**B** presents the attenuation data measured through such a thermocoax line within the same sample rod used for measuring stanene. A network analyzer with a frequency range of 300 kHz to 8.5 GHz was employed. The signal is strongly attenuated in the MHz/GHz range where the photon energy approximately corresponds to the measurement T through the relationship $hf = k_B T$. A flexible loom of superconducting NbTi wires is employed to connect the thermocoax cables, thermalized near the 1K stage, with the sample stage located in the mixture. The measurement electronics is powered by a dedicated phase of a three-phase power supply, operated on individual isolating transformers, and are isolated from the data gathering measurement computer by an optical isolator. Significant efforts, such as electrically isolating the cryostat from pumps and diagnostics electronics, have been taken to minimize ground-loops within the measurement circuitry. This setup has proven extremely effective in the study of delicate fractional quantum Hall phases *(32-35)* whose activation gaps are on the order of 100 mK, and were observed to continue to develop down to base T of the cryostat, suggesting good coupling

between the two-dimensional electron gas electron temperature and that indicated by the mixing chamber thermometer. During the measurements, the stanene devices were excited with a low frequency AC current of $I \leqslant 100$ nA ($I \ll I_c$, where I_c is the critical superconducting current), with the local voltage drop being measured in a four-point configuration using a SR830 lock-in amplifier.

II. Estimation of the mean free path and the coherence length

The band structure of a stanene trilayer as measured by ARPES, consists of a hole band with a linear dispersion and a small electron pocket around the Γ-point. For 3-Sn/6-PbTe, the linear band plays a dominant role in transport, as has been shown in previous work *(21)*. We therefore estimate the mean free path l assuming that only this linear band contributes to transport. We start with the formula for the conductivity in the Drude picture,

$$\sigma = \frac{e^2 \tau n}{m},$$

where $\sigma = 1/R_{sheet}$. R_{sheet} is the sheet resistance of the sample, τ the scattering time, n the charge carrier density and m the effective mass. The carrier density can be calculated from the Fermi momentum k_F by $n = \frac{k_F^2}{2\pi}$ (assuming a degeneracy of two) and m from $\frac{\hbar k_F}{v_F}$, where v_F is the Fermi velocity *(34)(35)*. By using the relation $l = v_F \tau$, we obtain:

$$l = \frac{h/e^2}{R_{sheet}} \frac{1}{k_F}.$$

A normal state sheet resistance of 1 kΩ is used for the evaluation of l. From the ARPES data in our previous work *(21)*, the Fermi momentum was determined to be 0.25 $Å^{-1}$. The calculated mean free path then equals 10 nm. We note that this estimate yields an upper bound of l because additional bands with linear dispersion cross the Fermi level. The evaluated mean free path is consistent with that calculated by directly multiplying the Fermi velocity obtained from ARPES ($v_F \sim 5 \times 10^4$ m/s *(21)*) and the scattering time estimated from a fit of the temperature dependent in-plane upper critical field with the theoretical model (τ_0 ~0.05 ps in Table S1): $v_F \tau_0$~2.5 nm.

The superconducting coherence length ξ is obtained with the help of the two-dimensional Ginzburg-Landau formula

$$\xi = \sqrt{\frac{\Phi_0/2\pi}{-dB_{c2}/dT \cdot T_{c,0}}}.$$

Here, $-dB_{c2}/dT$ is the slope of the temperature dependence of the out-of-plane B_{c2} data close to $T_{c,0}$ (dotted lines in Fig. S3 to S6). We obtain a coherence length of 54 nm for 3-Sn/6-PbTe. The values of ξ for other samples are included in the corresponding figure captions. The above coherence length has been extracted based on the criterion that the critical field occurs when the resistance has dropped to 50% of the normal state resistance. If a more stringent criterion is used, such as for instance 1% of the normal state resistance, the critical field becomes smaller such that $-dB_{c2}/dT \cdot T_{c,0}$ is reduced. Consequently, the coherence length is larger and equal to 80 nm.

III. Comparison with the FFLO state

Superconductors based on the FFLO state can exhibit an up-turn in $B_{c2}(T)$ at low temperatures *(16-19)*. However, the FFLO state is very sensitive to impurity scattering and requires the superconductor to be clean, i.e. the mean free path l should exceed the coherence length ξ. Based on the estimate above, few-layer stanene is however still not a clean superconductor. We also made an attempt to fit the experimental data with the 2D FFLO B_{c2} formula *(16)* as shown in Fig. 2**E** and Fig. S3**D**-S6**D** and obtain poor agreement. Finally, we note that Rashba spin-orbit coupling (SOC) has an opposite effect on the 2D FFLO state and the type-II Ising pairing proposed here. As shown in ref. *(18)*, the Rashba SOC can prominently enhance B_{c2} at low temperatures for the superconductor hosting the FFLO state. This is against our experimental observation that the up-turn feature gets smeared out in bilayer stanene (Fig. 3 **B**) in which the Rashba SOC should be more pronounced than that in the stanene trilayer or penta-layer.

IV. Anisotropic g-factor

The formula $B_p = 1.86T_c$ for calculating the Pauli limit assumes a g-factor of 2. However, in quasi-2D systems, there can be a strong anisotropy of the g-factor *(36)*. An ideal two-dimensional system with no dispersion along the out-of-plane direction (z-direction) has $1/m_z^* = 0$. As a consequence, the in-plane g-factor, which is proportional to $1/m_z^*$, has to be zero. A quasi-2D system with a finite thickness still has weak dispersion along the z-direction, giving rise to a finite

$1/m_z^*$ and hence non-zero in-plane g-factor: $g_\parallel$. Due to the strong anisotropy, $g_\parallel$ can be greatly suppressed relative to the out-of-plane g-factor. However, it may still possess an absolute value that is comparable with the g-factor of a free electron. For free-standing trilayer stanene, we obtain from first-principles calculations that the in-plane (out-of-plane) g-factors are 1.4 (33), 1.8 (4.6) at $E - E_F =$ -0.1, -0.2 eV. These theoretically chosen energy positions are close to the Fermi levels in the experimental situations under different doping *(21)*. The large in-plane g-factors indicate that trilayer stanene is in the bulk limit. In comparison, we estimate—based on the out-of-plane upper critical fields in Fig. S4 **C** and Fig. 2 **D**—that the upper bound for the out-of-plane g-factors are 9.9 and 7.0, respectively. The numerical value of 33 is larger than the estimated value of 9.9 from experiment. Apart from the uncertainty in the numerical evaluation, this difference may indicate that our few-layer stanene possesses a larger gap to T_c ratio than the standard BCS ratio of $\triangle/k_B T_{c,0} =$1.76.

V. Theoretical model

Based on previous studies *(23, 39, 40)*, the four-band model with the basis ($p_{x+iy,\uparrow}$, $p_{x-iy,\uparrow}$, $p_{x-iy,\downarrow}$, $p_{x+iy,\downarrow}$) and the external magnetic field B applied along the x-axis produces the following Hamiltonian:

$$H = Ak^2 + \begin{bmatrix} H_+(k) & -\mu_B B\sigma_x \\ -\mu_B B\sigma_x & H_-(k) \end{bmatrix}. \qquad \text{(S1)}$$

Here $H_\pm(k) = (M_0 - M_1 k^2)\sigma_z + v(\pm k_x\sigma_x + k_y\sigma_y)$. σ_x, σ_y and σ_z are the Pauli matrices. k_x and k_y are the momenta in the plane of the 2D superconductor. μ_B is the Bohr magneton. The energy dispersion is determined by the mass parameter M_0, the Fermi velocity v and the material specific constants M_1 and A. The zero-field version of this Hamiltonian is the Bernevig-Hughes-Zhang Hamiltonian for the 2D topological insulator *(39)*. The Zeeman terms were considered in ref. *(40)*. We consider first the situation where only a single band crosses the Fermi level. The critical field B_{c2} can be solved within the Werthamer-Helfand-Hohenberg (WHH) framework *(41)*. We derive the temperature dependence of the in-plane upper critical field with the help of the Gor'kov Green function:

$$ln\frac{T_c}{T_{c,0}}+\frac{\mu_B^2B^2}{\beta_{so}^{*2}+\mu_B^2B^2}Re\left[\psi\left(\frac{1}{2}+\frac{i\sqrt{\beta_{so}^{*2}+\mu_B^2B^2}}{2\pi k_BT_c}\right)-\psi\left(\frac{1}{2}\right)\right]=0, \quad \text{(S2)}$$

where $\beta_{so}^{*}=\frac{\sqrt{\left(M_0-M_1k_F^2\right)^2+v^2k_F^2}}{1+\hbar/2\pi\tau_0\cdot k_BT_{c,0}}$ is the disorder renormalized SOC strength. k_F denotes the Fermi momentum, ψ the digamma function and τ_0 the scattering time.

In the case where Rashba SOC cannot be neglected, an additional term needs to be considered in the Hamiltonian: $H_R=-\alpha\left(k_y\sigma_x^{'}-k_x\sigma_y^{'}\right)\sigma_x$. Here, α denotes the Rashba SOC strength, and $\sigma^{'}$ and σ represent the Pauli matrices for real spin and pseudo-spin, respectively. The temperature dependence then becomes:

$$ln\frac{T_c}{T_{c,0}}+\frac{1}{2}(G_++G_-)-\psi\left(\frac{1}{2}\right)=0, \quad \text{(S3)}$$

with $G_\pm=\left(1\mp\frac{2(\alpha k_F)^2+\beta_{so}^{*2}-\mu_B^2B^2}{\rho_+^2-\rho_-^2}\right)Re\left[\psi\left(\frac{1}{2}+\frac{i\rho_\pm}{2\pi k_BT_c}\right)\right]$ and $2\rho_\pm=\sqrt{(\mu_BB+\alpha k_F)^2+(\alpha k_F)^2+\beta_{so}^{*2}}\pm\sqrt{(\mu_BB-\alpha k_F)^2+(\alpha k_F)^2+\beta_{so}^{*2}}$. Here, αk_F denotes the disorder renormalized Rashba SOC strength.

In the more realistic situation where M_0, M_1, A and v give rise to the inverted Mexican hat shaped band of few-layer stanene, there are two bands crossing the Fermi level. We can join the single band formula in virtue of the quasi-classical two-band Usadel equations *(22)*. The final equation that governs the temperature dependence of the critical field is

$$\frac{2w}{\lambda_0}F_1F_2+\left(1+\frac{\lambda_-}{\lambda_0}\right)F_1+\left(1+\frac{\lambda_-}{\lambda_0}\right)F_2=0, \text{(S4)}$$

with $F_j = ln\frac{T_c}{T_{c,0}} + \frac{1}{2}\left(G_{+,j} + G_{-,j}\right) - \psi\left(\frac{1}{2}\right)$, $G_{\pm,j} = \left(1 \mp \frac{2(\alpha_j k_{F,j})^2 + \beta_{so,j}^{*2} - \mu_B^2 B^2}{\rho_{+,j}^2 - \rho_{-,j}^2}\right) Re\left[\psi\left(\frac{1}{2} + \frac{i\rho_{\pm,j}}{2\pi k_B T_c}\right)\right]$ and $j = 1,2$. λ_{11}, λ_{22} and λ_{12} represent the BCS electron-phonon coupling constants, $\lambda_\pm = \lambda_{11} \pm \lambda_{22}$, $\lambda_0 = \sqrt{\lambda_-^2 + 4\lambda_{12}^2}$ and $w = \lambda_{11}\lambda_{22} - \lambda_{12}^2$.

In order to minimize the number of fit parameters, we employ equations (S2) and (S3) to fit our experimental data. This is valid because equation (S4) reduces to the single band form if the two bands have similar SOC or one band dominates (neglecting interband scattering).

The extracted fit parameters are summarized in Table S1. We estimate τ_0 by setting the renormalization factor $1 + \hbar/(2\pi\tau_0 \cdot k_B T_{c,0}) = 50$, which accounts for the reduced SOC strength β_{so}^* from the pure component originating from the electronic bands β_{so}. The estimated τ_0 in few-layer stanene is comparable to that of MoS_2 in previous studies *(3)*.

For the perpendicular upper critical field, we use the following formula *(22)* to fit the data

$$\ln\frac{T_c}{T_{c,0}} = -\frac{\left[U\left(\frac{eD_1B}{hT_c}\right) + U\left(\frac{eD_2B}{hT_c}\right) + \frac{\lambda_0}{w}\right]}{2} + \left[\frac{\left(U\left(\frac{eD_1B}{hT_c}\right) - U\left(\frac{eD_2B}{hT_c}\right) - \frac{\lambda_-}{w}\right)^2}{4} + \frac{\lambda_{12}^2}{w^2}\right]^{\frac{1}{2}}. \quad \text{(S5)}$$

Here, $U(x) = \psi\left(\frac{1}{2} + x\right) - \psi\left(\frac{1}{2}\right)$ with ψ the digamma function. D_1 and D_2 are the diffusivities of the two bands.

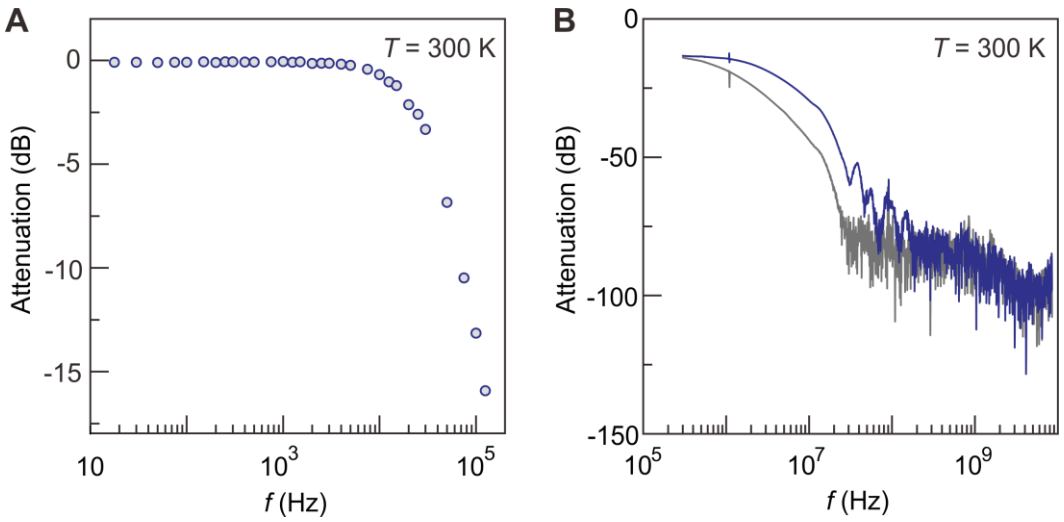

Fig. S1. Transmission characteristics of measurement lines. A characteristics of the low-pass filter in the breakout box of the measurement system. **B** attenuation from the breakout box to the sample stage along the thermocoax line without (blue) or with (gray) the low-pass filter.

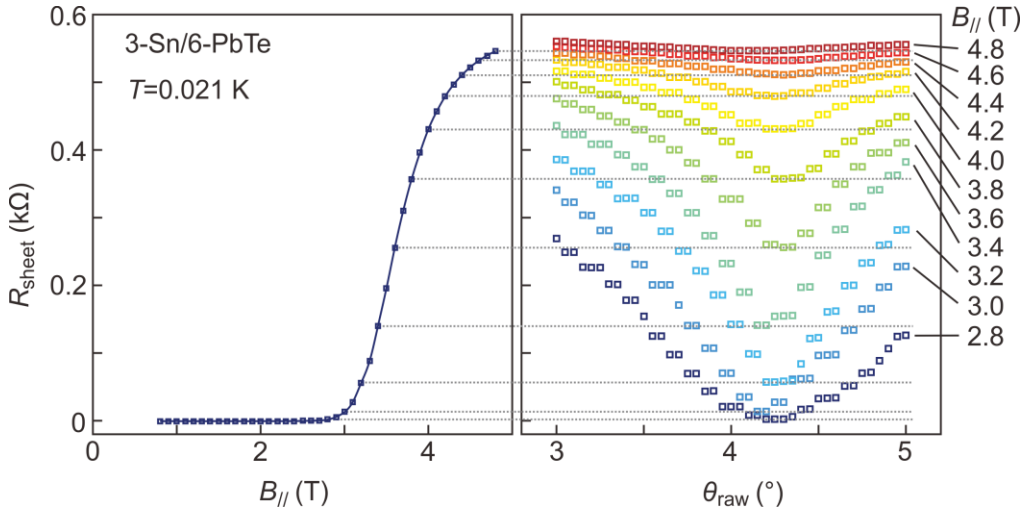

Fig. S2. Illustration of the data points taken in the in-plane situation. For each curve shown in panel **B** of Fig. S4-S6, we fix the temperature and record the resistance as a function of rotation angle around the in-plane situation at a set of magnetic fields. The right panel exemplifies the obtained data. We take the minimum resistance in each rotation as one data point of the resistance at fixed $\boldsymbol{B_{c2,\parallel}}$ and $\boldsymbol{T}$. The solid curve in the left panel is obtained by interpolation.

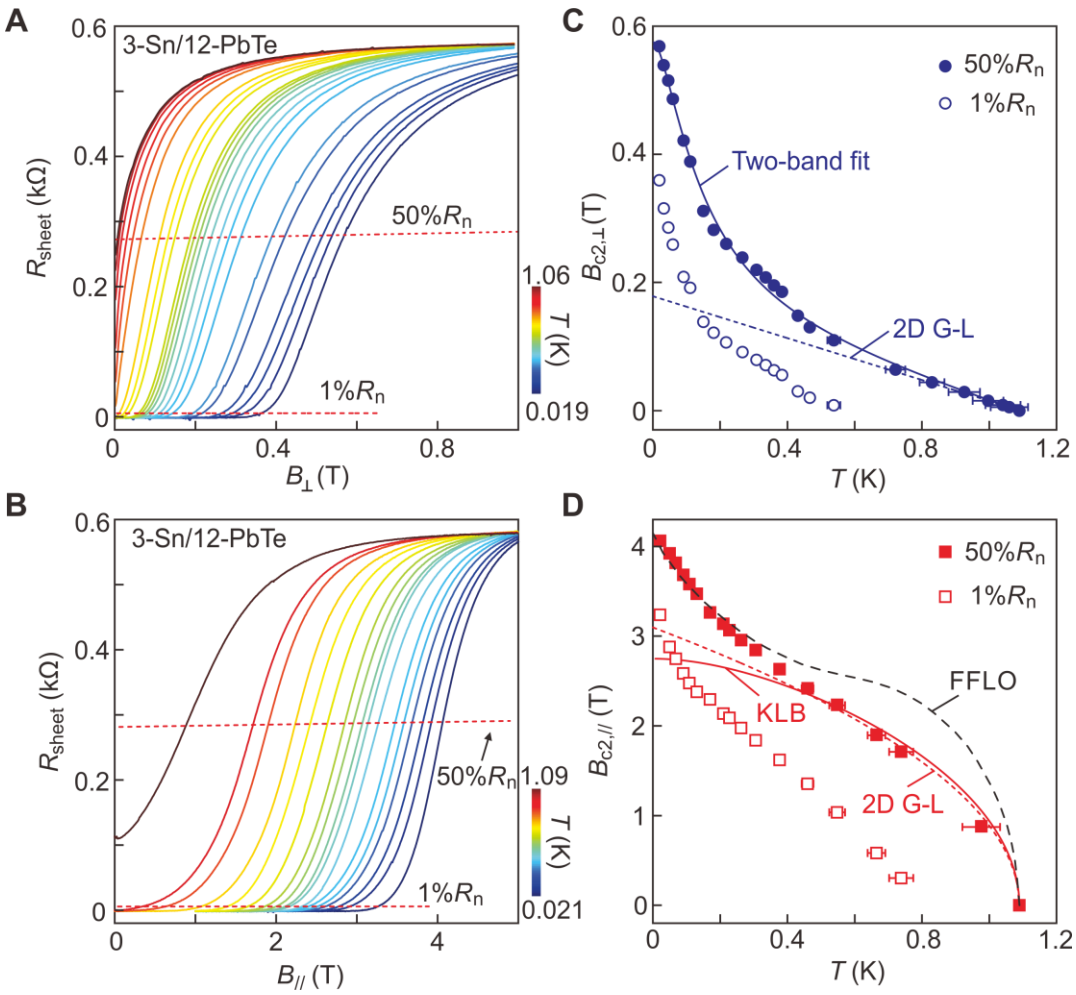

Fig. S3. Magneto-transport data on a 3-Sn/12-PbTe sample. A, B: Sheet resistances as a function of out-of-plane/in-plane magnetic fields at a set of temperatures. The upper critical fields are obtained from the position where the resistance drops to either half or 1% of its normal state resistance (indicated by the red dotted line). **C, D:** Temperature dependence of the out-of-plane/in-plane upper critical fields. Horizontal error bars stem from the temperature variation during each scan of the resistance data. Errors are smaller than the symbols for those data points without apparent error bars. The dotted curves in (C) and (D) are fits using the two-dimensional Ginzburg-Landau equations *(4)*, yielding a coherence length $\boldsymbol{\xi = 43}$ nm and a superconductor thickness $\boldsymbol{d_{SC} = 8.6}$ nm. Solid curve in (C) is a fit obtained by employing the two-band formula of Eq. (S4) *(23)*. The solid curve in (D) results from the KLB formula *(10)*. The dashed curve in (D) is a fit to the FFLO formula *(16)*.

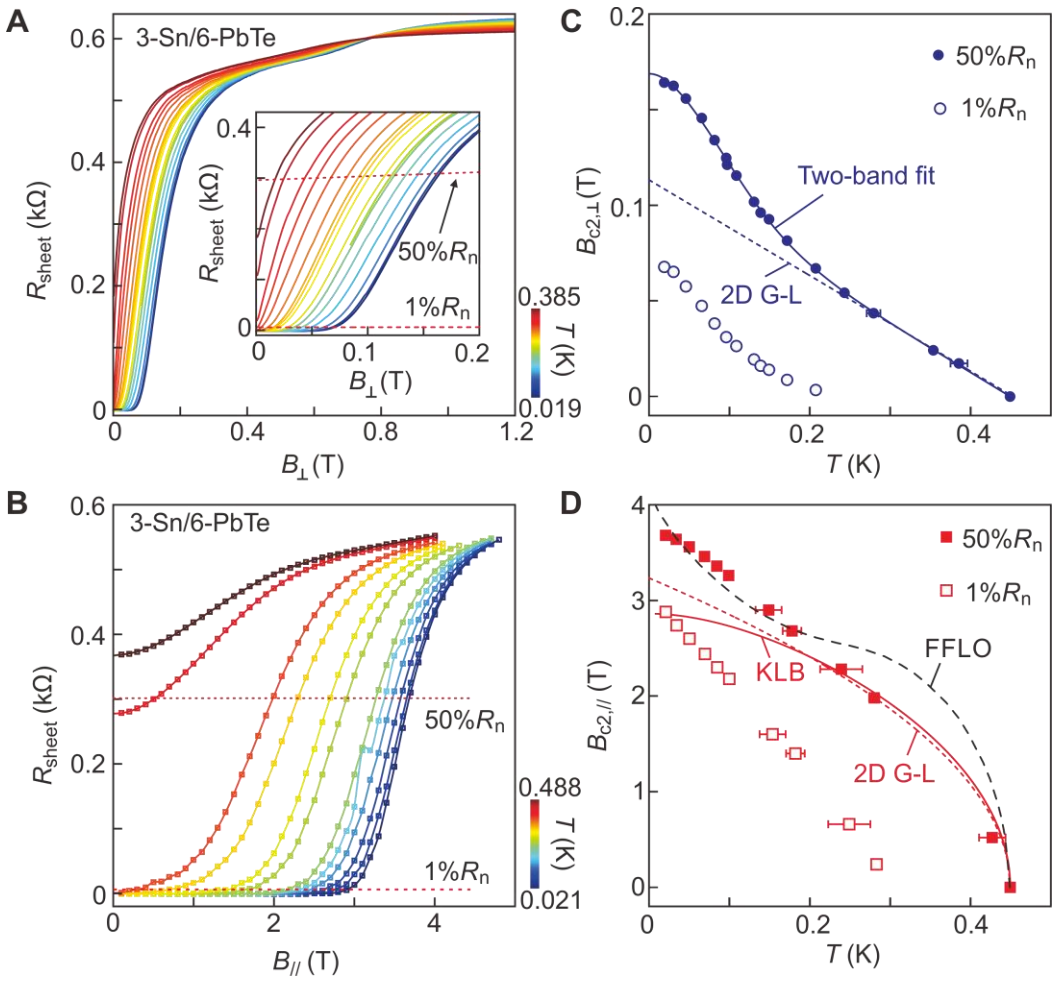

Fig. S4. Magneto-transport data on a 3-Sn/6-PbTe sample. A, B: Sheet resistances as a function of out-of-plane/in-plane magnetic fields at a set of temperatures. Solid curves in **B** are obtained by interpolation. The upper critical fields are determined from the position where the resistance drops to either half or 1% of its normal state resistance (indicated by the red dotted line). **C, D**: Temperature dependence of the out-of-plane/in-plane upper critical fields. Horizontal error bars stem from the temperature variation during each scan of the resistance data. Errors are smaller than the symbols for those data points without apparent error bars. The dotted curves in (C) and (D) are fits using the two-dimensional Ginzburg-Landau equations *(4)*, yielding a coherence length $\boldsymbol{\xi = 54}$ nm and a superconductor thickness $\boldsymbol{d_{SC} = 6.8}$ nm. The solid curve in (C) is a fit employing the two-band formula of Eq. (S4) *(23)*. The solid curve in (D) results from the KLB formula *(10)*. The dashed curve in (D) is a fit to the FFLO formula *(16)*.

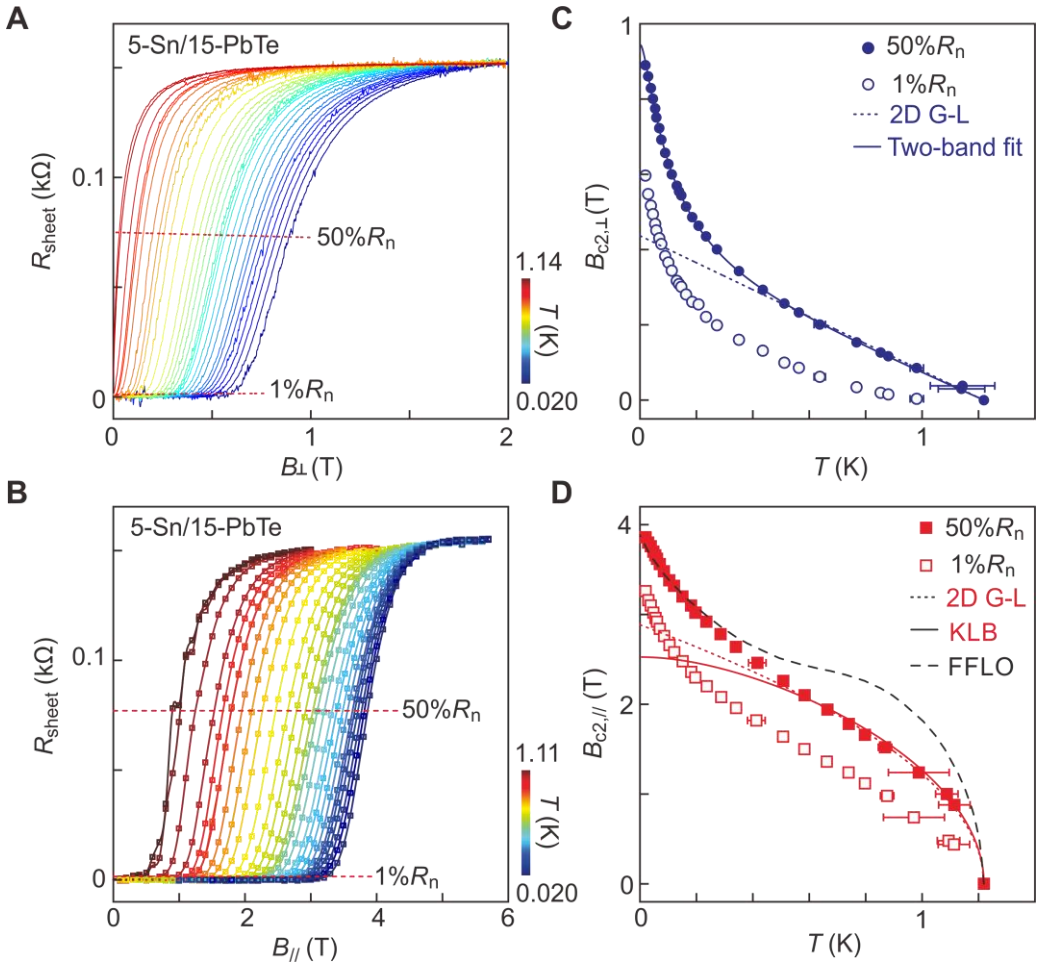

Fig. S5. Magneto-transport data on a 5-Sn/15-PbTe sample. A, B: Sheet resistances as a function of out-of-plane/in-plane magnetic fields at a set of temperatures. Solid curves in **B** are obtained by interpolation. The upper critical fields are determined from the position where the resistance drops to either half or 1% of its normal state resistance (indicated by the red dotted line). **C, D**: Temperature dependence of the out-of-plane/in-plane upper critical fields. Horizontal error bars stem from the temperature variation during each scan of the resistance data. Errors are smaller than the symbols for those data points without apparent error bars. The dotted curves in (C) and (D) are fits using the two-dimensional Ginzburg-Landau equations *(4)*, yielding a coherence length $\boldsymbol{\xi = 27}$ nm and a superconductor thickness $\boldsymbol{d_{SC} = 14}$ nm. The solid curve in (C) is a fit employing the two-band formula of Eq. (S4) *(23)*. The solid curve in (D) results from the KLB formula *(10)*. The dashed curve in (D) is a fit to the FFLO formula *(16)*.

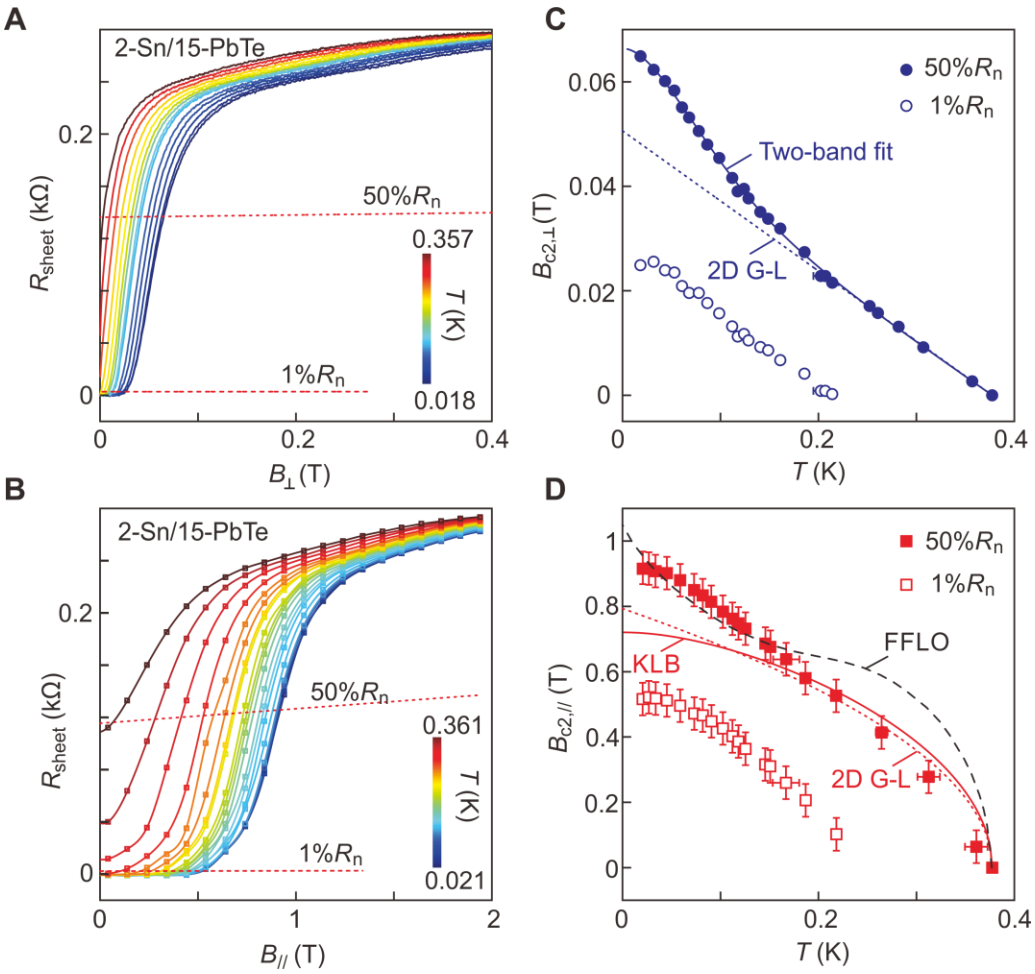

Fig. S6. Magneto-transport data on a 2-Sn/15-PbTe sample. A, B: Sheet resistances as a function of out-of-plane/in-plane magnetic fields at a set of temperatures. Solid curves in **B** are obtained by interpolation. The upper critical fields are determined from the position where the resistance drops to either half or 1% of its normal state resistance (indicated by the red dotted line). **C, D**: Temperature dependence of the out-of-plane/in-plane upper critical fields. Horizontal error bars stem from the temperature variation during each scan of the resistance data. Errors are smaller than the symbols for those data points without apparent error bars. The dotted curves in (C) and (D) are fits using the two-dimensional Ginzburg-Landau equations *(4)*, yielding a coherence length $\boldsymbol{\xi = 81}$ nm and a superconductor thickness $\boldsymbol{d_{SC} = 4.4}$ nm. The solid curve in (C) is a fit employing the two-band formula of Eq. (S4) *(23)*. The solid curve in (D) results from the KLB formula *(10)*. The dashed curve in (D) is a fit to the FFLO formula *(16)*.

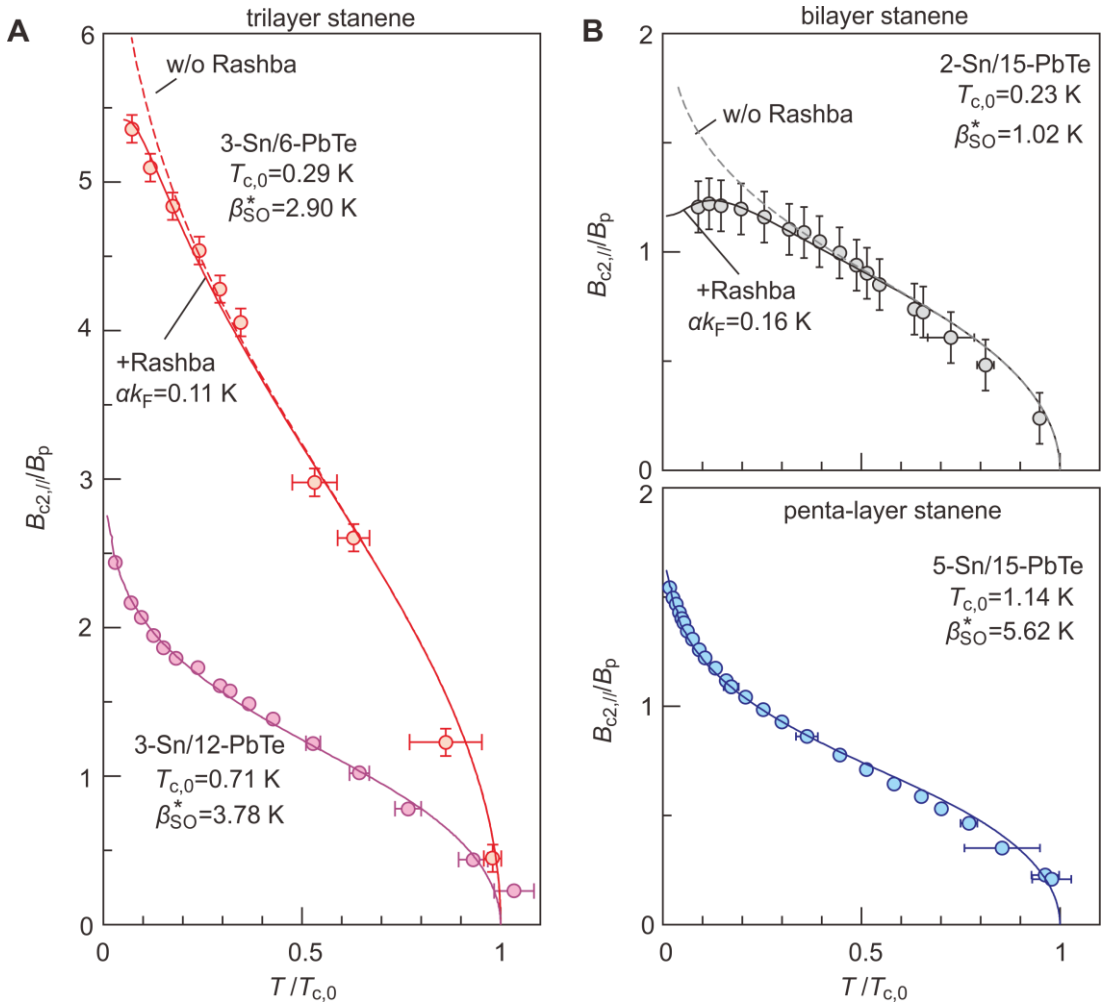

Fig. S7. Temperature dependence of the in-plane upper critical fields in few-layer stanene samples. Here, the upper critical field values are obtained from the positions where the resistance drops to 1% of the normal state resistance ($\boldsymbol{R_n}$) in the magnetic field sweeps at a set of temperature points. Vertical error bars arise from the step size of the magnetic field in obtaining the resistance data (explained in Fig. S2). Horizontal error bars stem from the temperature variation during each scan of the resistance data. Errors are smaller than the symbols for those data points without apparent error bars. Solid and dashed curves are theoretical fits by using Eq. (S2) and Eq. (S3). The fitted parameters are listed in the panels. Taking the criterion of 1%$\boldsymbol{R_n}$ affects the extracted values quantitatively, however, the general thickness dependence of them remains qualitatively the same as the seen in Fig. 3 where the criterion of 50%$\boldsymbol{R_n}$ is employed.

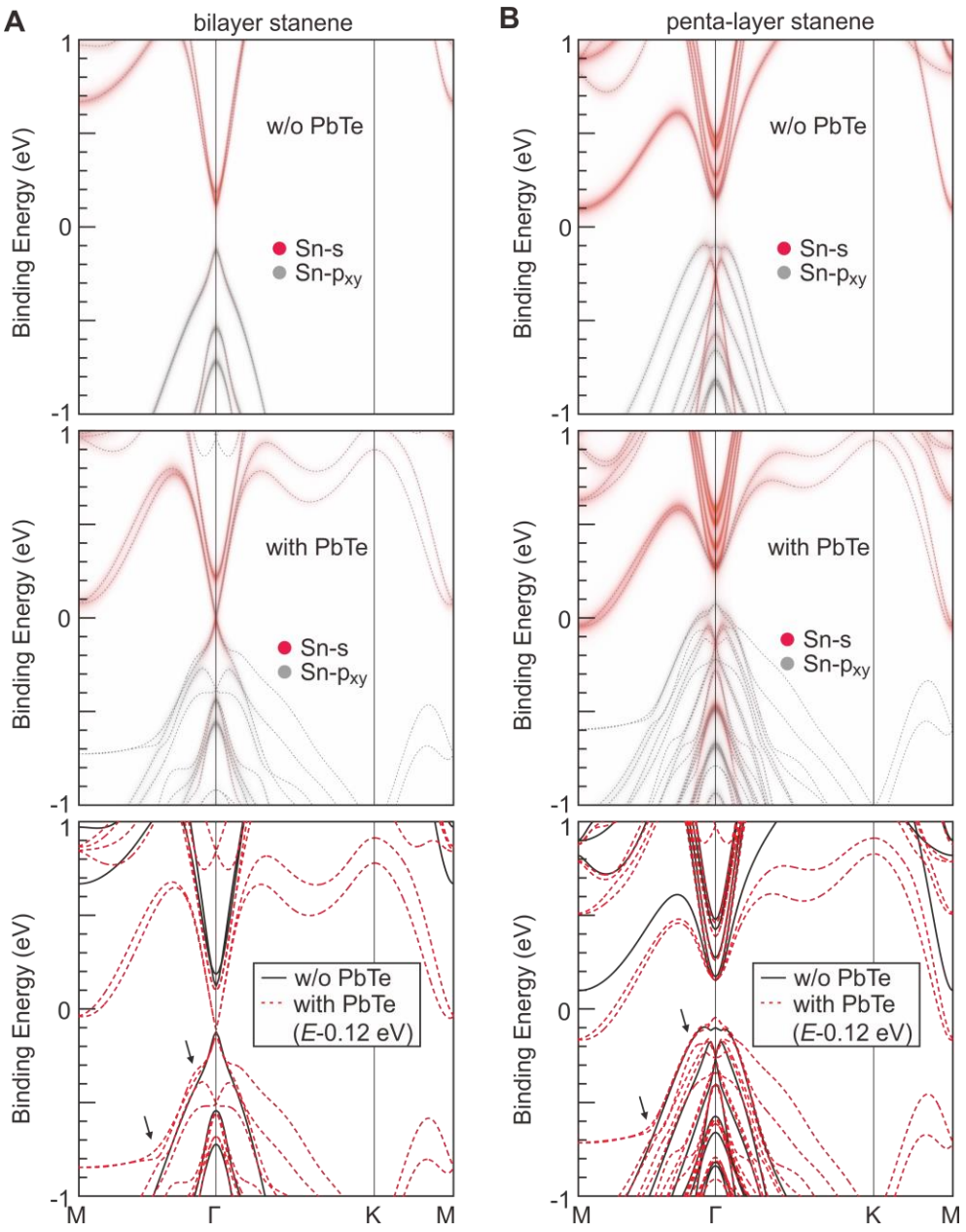

Fig. S8. First-principles calculations of 2-Sn and 5-Sn with and without the PbTe substrate. We perform the calculations with the Vienna ab initio simulation package, using the projector-augmented-wave potential, the Pedrew-Burke-Ernzerhof exchange-correlation functional and the plane-wave basis with an energy cut-off of 400 eV. Details are given before *(20)(21)*. The top surfaces of both 2-Sn and 5-Sn are decorated by hydrogen atoms. For the situation without the PbTe substrate, the bottom surfaces are decorated by hydrogen as well in the calculation. The bottom surface of the simulated PbTe substrate is further saturated by fluorine. The two panels in the bottom compare the energy bands without (solid) or with (dashed) the PbTe substrate. Bands

from the latter situation were vertically lowered by 0.12 eV for comparison. Drastic changes can be seen for the bilayer stanene as a consequence of breaking the inversion symmetry by adding PbTe. The energy gap at $\boldsymbol{\Gamma}$-point is almost closed for 2-Sn/PbTe. Also, M-shaped/W-shaped bands occur in the valence/conduction bands due to the Rashba splitting. In comparison, 5-Sn/PbTe shows weaker effect imposed by the inversion symmetry breaking. For example, the energy gap at $\boldsymbol{\Gamma}$-point is only slightly affected. Furthermore, the specific band indicated by the two black arrows show smaller vertical splitting in 5-Sn/PbTe, if compared to the band indicated by the same method in 2-Sn/PbTe.

	$T_{c,0}$ exp. (K)	$T_{c,0}$ theory (K)	β_{so}^{*} (K)	β_{so}^{*} (meV)	β_{so} (meV)	αk_F (K)	τ_0 (ps)
2-Sn/15-PbTe	0.377	0.364	1.54	0.132	6.6	0.10	0.066
3-Sn/6-PbTe	0.449	0.451	4.34	0.374	18.7	0.14	0.054
3-Sn/12-PbTe	1.090	1.030	4.34	0.374	18.7	--	0.023
5-Sn/15-PbTe	1.219	1.190	4.70	0.405	20.3	--	0.020

Table S1. Extracted fit parameters of the four samples. $\boldsymbol{T_{c,0}}$ is the zero-field transition temperature. The experimental values are obtained by extrapolating the linear fit (2D G-L fitting) in panel **C** of Fig. S3-S6 to zero field. The chosen parameter values for the traces are slightly different from the experimental ones to obtain the best fit with Eq. (S2) and (S3). $\boldsymbol{\beta_{so}^{*}}$ is the disorder renormalized SOC strength, which is shown in both K and meV units. $\boldsymbol{\beta_{so}}$ is the corresponding intrinsic SOC strength, if assuming a renormalization factor of 50. $\boldsymbol{\alpha k_F}$ denotes the disorder renormalized Rashba SOC strength. $\boldsymbol{\tau_0}$ is the estimated scattering time. The extracted SOC strength $\boldsymbol{\beta_{SO}^{*}}$ in 2-Sn is only half of that in 3-Sn or 5-Sn. This may originate from enhanced interface scattering *(42)* due to reduced film thickness. This more strongly renormalizes the intrinsic SOC, $\boldsymbol{\beta_{SO}}$ (Note that the intrinsic $\boldsymbol{\beta_{SO}}$ for 2-Sn listed above is obtained by assuming the same renormalization factor of 50 as for other thicknesses.). Assuming an inverse relation between the interface scattering and film thickness *(42)*, this scattering effect strengthens by a factor of 1.5- to 2.5 when going from 3-Sn or 5-Sn to 2-Sn.

References and Notes

1. A. Gurevich, To use or not to use cool superconductors? *Nat. Mater.* **10**, 255–259 (2011). doi:10.1038/nmat2991 Medline

2. Y. Saito, T. Nojima, Y. Iwasa, Highly crystalline 2D superconductors. *Nat. Rev. Mater.* **2**, 16094 (2017). doi:10.1038/natrevmats.2016.94

3. J. M. Lu, O. Zheliuk, I. Leermakers, N. F. Q. Yuan, U. Zeitler, K. T. Law, J. T. Ye, Evidence for two-dimensional Ising superconductivity in gated MoS_2. *Science* **350**, 1353–1357 (2015). doi:10.1126/science.aab2277 Medline

4. Y. Saito, Y. Nakamura, M. S. Bahramy, Y. Kohama, J. Ye, Y. Kasahara, Y. Nakagawa, M. Onga, M. Tokunaga, T. Nojima, Y. Yanase, Y. Iwasa, Superconductivity protected by spin-valley locking in ion-gated MoS_2. *Nat. Phys.* **12**, 144–149 (2015). doi:10.1038/nphys3580

5. X. Xi, Z. Wang, W. Zhao, J.-H. Park, K. T. Law, H. Berger, L. Forró, J. Shan, K. F. Mak, Ising pairing in superconducting $NbSe_2$ atomic layers. *Nat. Phys.* **12**, 139–143 (2016). doi:10.1038/nphys3538

6. J. Lu, O. Zheliuk, Q. Chen, I. Leermakers, N. E. Hussey, U. Zeitler, J. Ye, Full superconducting dome of strong Ising protection in gated monolayer WS_2. *Proc. Natl. Acad. Sci. U.S.A.* **115**, 3551–3556 (2018). doi:10.1073/pnas.1716781115 Medline

7. S. C. de la Barrera, M. R. Sinko, D. P. Gopalan, N. Sivadas, K. L. Seyler, K. Watanabe, T. Taniguchi, A. W. Tsen, X. Xu, D. Xiao, B. M. Hunt, Tuning Ising superconductivity with layer and spin-orbit coupling in two-dimensional transition-metal dichalcogenides. *Nat. Commun.* **9**, 1427 (2018). doi:10.1038/s41467-018-03888-4 Medline

8. A. M. Clogston, Upper limit for the critical field in hard superconductors. *Phys. Rev. Lett.* **9**, 266–267 (1962). doi:10.1103/PhysRevLett.9.266

9. B. S. Chandrasekhar, A note on the maximum critical field of high-field superconductors. *Appl. Phys. Lett.* **1**, 7–8 (1962). doi:10.1063/1.1777362

10. R. A. Klemm, A. Luther, M. R. Beasley, Theory of the upper critical field in layered superconductors. *Phys. Rev. B* **12**, 877–891 (1975). doi:10.1103/PhysRevB.12.877

11. S. Ilić, J. S. Meyer, M. Houzet, Enhancement of the upper critical field in disordered transition metal dichalcogenide monolayers. *Phys. Rev. Lett.* **119**, 117001 (2017). doi:10.1103/PhysRevLett.119.117001 Medline

12. Y. Liu, Z. Wang, X. Zhang, C. Liu, Y. Liu, Z. Zhou, J. Wang, Q. Wang, Y. Liu, C. Xi, M. Tian, H. Liu, J. Feng, X. C. Xie, J. Wang, Interface-induced Zeeman-protected superconductivity in ultrathin crystalline lead films. *Phys. Rev. X* **8**, 021002 (2018). doi:10.1103/PhysRevX.8.021002

13. R. Wakatsuki, K. T. Law, Proximity effect and Ising superconductivity in superconductor/transition metal dichalcogenide heterostructures. arXiv:1604.04898 [cond-mat.supr-con] (2016).

14. P. Fulde, R. A. Ferrell, Superconductivity in a strong spin-exchange field. *Phys. Rev.* **135** (3A), A550–A563 (1964). doi:10.1103/PhysRev.135.A550

15. A. I. Larkin, Yu. N. Ovchinnikov, Inhomogeneous state of superconductors. *Sov. Phys. JETP* **20**, 762 (1965).

16. H. Shimahara, Fulde-Ferrell state in quasi-two-dimensional superconductors. *Phys. Rev. B Condens. Matter* **50**, 12760–12765 (1994). doi:10.1103/PhysRevB.50.12760 Medline

17. Y. Matsuda, H. Shimahara, Fulde-Ferrell-Larkin-Ovchinnikov state in heavy fermion superconductors. *J. Phys. Soc. Jpn.* **76**, 051005 (2007). doi:10.1143/JPSJ.76.051005

18. G. Zwicknagl, S. Jahns, P. Fulde, Critical magnetic field of ultra-thin superconducting films and interfaces. *J. Phys. Soc. Jpn.* **86**, 083701 (2017). doi:10.7566/JPSJ.86.083701

19. J. Wosnitza, FFLO states in layered organic superconductors. *Ann. Phys.* **530**, 1700282 (2018). doi:10.1002/andp.201700282

20. Y. Zang, T. Jiang, Y. Gong, Z. Guan, C. Liu, M. Liao, K. Zhu, Z. Li, L. Wang, W. Li, C. Song, D. Zhang, Y. Xu, K. He, X. Ma, S.-C. Zhang, Q.-K. Xue, Realizing an epitaxial decorated stanene with an insulating bandgap. *Adv. Funct. Mater.* **28**, 1802723 (2018). doi:10.1002/adfm.201802723

21. M. Liao, Y. Zang, Z. Guan, H. Li, Y. Gong, K. Zhu, X.-P. Hu, D. Zhang, Y. Xu, Y.-Y. Wang, K. He, X.-C. Ma, S.-C. Zhang, Q.-K. Xue, Superconductivity in few-layer stanene. *Nat. Phys.* **14**, 344–348 (2018). doi:10.1038/s41567-017-0031-6

22. A. Gurevich, Limits of the upper critical field in dirty two-gap superconductors. *Physica C* **456**, 160–169 (2007). doi:10.1016/j.physc.2007.01.008

23. Y. Xu, B. Yan, H.-J. Zhang, J. Wang, G. Xu, P. Tang, W. Duan, S.-C. Zhang, Large-gap quantum spin Hall insulators in tin films. *Phys. Rev. Lett.* **111**, 136804 (2013). doi:10.1103/PhysRevLett.111.136804 Medline

24. Y. Xu, Z. Gan, S.-C. Zhang, Enhanced thermoelectric performance and anomalous seebeck effects in topological insulators. *Phys. Rev. Lett.* **112**, 226801 (2014). doi:10.1103/PhysRevLett.112.226801 Medline

25. C. Wang, B. Lian, X. Guo, J. Mao, Z. Zhang, D. Zhang, B.-L. Gu, Y. Xu, W. Duan, Type-II Ising superconductivity in two-dimensional materials with strong spin-orbit coupling. *Phys. Rev. Lett.* **123**, 126402 (2019). doi:10.1103/PhysRevLett.123.126402 Medline

26. Y. Liu, Y. Xu, J. Sun, C. Liu, Y. Liu, C. Wang, Z. Zhang, K. Gu, Y. Tang, C. Ding, H. Liu, H. Yao, X. Lin, L. Wang, Q. Xue, J. Wang, Quantum metal state and quantum phase transitions in type-II Ising superconducting films. arXiv:1904.12719 [cond-mat.supr-con] (2019).

27. A. Devarakonda, H. Inoue, S. Fang, C. Ozsoy-Keskinbora, T. Suzuki, M. Kriener, L. Fu, E. Kaxiras, D. C. Bell, J. G. Checkelsky, Evidence for clean 2D superconductivity and field-induced finite-momentum pairing in a bulk vdW superlattice. arXiv:1906.02065 [cond-mat.supr-con] (2019).

28. D. Zhang, Data for "Type-II Ising superconductivity in few-layer stanene". Harvard Dataverse (2020); doi:10.7910/DVN/O38NC2

29. I. Tamir, A. Benyamini, E. J. Telford, F. Gorniaczyk, A. Doron, T. Levinson, D. Wang, F. Gay, B. Sacépé, J. Hone, K. Watanabe, T. Taniguchi, C. R. Dean, A. N. Pasupathy, D.

Shahar, Sensitivity of the superconducting state in thin films. *Sci. Adv.* **5**, eaau3826 (2019). doi:10.1126/sciadv.aau3826 Medline

30. A. B. Zorin, The thermocoax cable as the microwave frequency filter for single electron circuits. *Rev. Sci. Instrum.* **66**, 4296–4300 (1995). doi:10.1063/1.1145385

31. J. Gores, thesis, University of Stuttgart, 2004.

32. J. Falson, D. Tabrea, D. Zhang, I. Sodemann, Y. Kozuka, A. Tsukazaki, M. Kawasaki, K. von Klitzing, J. H. Smet, A cascade of phase transitions in an orbitally mixed half-filled Landau level. *Sci. Adv.* **4**, eaat8742 (2018). doi:10.1126/sciadv.aat8742 Medline

33. D. Zhang, W. Dietsche, K. von Klitzing, Anomalous interlayer transport of quantum Hall bilayers in the strongly Josephson-coupled regime. *Phys. Rev. Lett.* **116**, 186801 (2016). doi:10.1103/PhysRevLett.116.186801 Medline

34. J. Falson, D. Maryenko, B. Friess, D. Zhang, Y. Kozuka, A. Tsukazaki, J. H. Smet, M. Kawasaki, Even-denominator fractional quantum Hall physics in ZnO. *Nat. Phys.* **11**, 347–351 (2015). doi:10.1038/nphys3259

35. D. Zhang, X. Huang, W. Dietsche, K. von Klitzing, J. H. Smet, Signatures for Wigner crystal formation in the chemical potential of a two-dimensional electron system. *Phys. Rev. Lett.* **113**, 076804 (2014). doi:10.1103/PhysRevLett.113.076804 Medline

36. A. H. Castro Neto, F. Guinea, N. M. R. Peres, K. S. Novoselov, A. K. Geim, The electronic properties of graphene. *Rev. Mod. Phys.* **81**, 109–162 (2009). doi:10.1103/RevModPhys.81.109

37. A. S. Mayorov, R. V. Gorbachev, S. V. Morozov, L. Britnell, R. Jalil, L. A. Ponomarenko, P. Blake, K. S. Novoselov, K. Watanabe, T. Taniguchi, A. K. Geim, Micrometer-scale ballistic transport in encapsulated graphene at room temperature. *Nano Lett.* **11**, 2396–2399 (2011). doi:10.1021/nl200758b Medline

38. A. Zhao, J. Zhang, Q. Gu, R. A. Klemm, A relativistic electron in an anisotropic conduction band. arXiv:1905.03127 [cond-mat.str-el] (2019).

39. B. A. Bernevig, T. L. Hughes, S.-C. Zhang, Quantum spin Hall effect and topological phase transition in HgTe quantum wells. *Science* **314**, 1757–1761 (2006). doi:10.1126/science.1133734 Medline

40. M. König, H. Buhmann, L. W. Molenkamp, T. Hughes, C.-X. Liu, X.-L. Qi, S.-C. Zhang, The quantum spin Hall effect: Theory and experiment. *J. Phys. Soc. Jpn.* **77**, 031007 (2008). doi:10.1143/JPSJ.77.031007

41. N. R. Werthamer, E. Helfand, P. C. Hohenberg, Temperature and purity dependence of the superconducting critical field H_{c2}. *Phys. Rev.* **147**, 295–302 (1966). doi:10.1103/PhysRev.147.295

42. D. Yue, X. Jin, Towards a better understanding of the anomalous Hall effect. *J. Phys. Soc. Jpn.* **86**, 011006 (2017). doi:10.7566/JPSJ.86.011006